Contents lists available at ScienceDirect

Engineering Fracture Mechanics

journal homepage: www.elsevier.com/locate/engfracmech



The influence of specimen length on the residual stress and fatigue life

Jorrit Rodenburg ^a, Henk Slot ^a, Sjoerd Hengeveld ^{a,b}, Johan Maljaars ^{a,b},

ARTICLE INFO

Keywords: Size effect Finite element analysis Welding simulation Residual stress Fatigue life

ABSTRACT

This paper studies the influence of specimen length on residual stress redistribution and fatigue life in welded cruciform joints made of steel grade S355. It uses numerical methods to simulate the common practice in fatigue testing, where specimens are cut from a larger welded plate assembly. A transient thermo-mechanical finite element model is used to simulate the welding and cutting processes, enabling a detailed analysis of residual stress relaxation due to reduced structural constraints when cutting the specimens. Fatigue life is assessed using linear elastic fracture mechanics, incorporating residual stress effects from the finite element simulations via a mean stress correction. Results show that shorter specimens exhibit reduced residual stress and increased fatigue resistance. For assemblies with a single pass weld, a minimum specimen length of 40 mm is recommended for deriving reliable S-N curves for welded joints in fatigue standards. The findings are in good agreement with experimental data and highlight the importance of specimen size in fatigue testing protocols.

1. Introduction

Residual stresses are present in steel structures after manufacturing. The most commonly used joining technique in steel construction, welding, results in residual stresses due to constrained expansion and shrinkage of steel caused by heating and cooling. Residual stresses influence the fatigue life of a structure similarly to an applied mean stress [1,2]. Hence, compressive residual stresses decrease the rate of fatigue crack nucleation and growth and are therefore beneficial for the fatigue life of a structure, while tensile residual stresses increase the rate of fatigue crack nucleation and growth and are therefore detrimental to the fatigue life of a structure.

S-N curves for fatigue verification are based on fatigue tests. Since fatigue tests on large steel assemblies are costly and can be difficult to interpret for general purposes, the specimens usually used for this purpose consist of single welded joints of limited length. To obtain multiple specimens and to prevent the effects of start-stop positions in each specimen, welded assemblies of larger lengths are usually manufactured and subsequently cut into multiple smaller specimens. The length of the weld included in the test specimen affects its fatigue resistance. As an illustration, Fig. 1 presents the fatigue strength at $N=2\cdot 10^6$ cycles $\Delta\sigma_{2e6}$ as a function of the specimen length L taken from several studies. The applied stress ratio R_{load} and specimen type vary per study, both of which affect the fatigue strength. Note that Deinböck and Baumgartner reported the effective notch stress and the length of the weld that is above 80% ($L_{80\%}$) or 90% ($L_{90\%}$) of the maximum stress in the weld [3,4]. Also note that Deinböck presents the fatigue strength at $N = 7 \cdot 10^5$ cycles, which is converted to $\Delta \sigma_{2e6}$ using an S–N curve slope of m = -3 [3]. The specimen length will

https://doi.org/10.1016/j.eng fracmech. 2025.111581

Received 18 June 2025; Received in revised form 22 August 2025; Accepted 25 September 2025

Available online 30 September 2025

0013-7944/© 2025 The Authors. Published by Elsevier Ltd. This is an open access article under the CC BY license (http://creativecommons.org/licenses/by/4.0/).

a TNO. Molengraaffsingel 8. Delft. 2629 JD. The Netherlands

^b Eindhoven University and Technology, Groene Loper 3, Eindhoven, 5612 AE, The Netherlands

Corresponding author at: Eindhoven University and Technology, Groene Loper 3, Eindhoven, 5612 AE, The Netherlands. E-mail address: johan.maljaars@tno.nl (J. Maljaars).

Nomenclature	
Greek symbols	
α	Linear expansion coefficient
ΔK	Stress intensity factor range
$\Delta\epsilon$	Strain increment
$\Delta\sigma_{2e6}$	Fatigue strength at 2e6 cycles
η	Efficiency
ρ	Density
σ_B	Stefan–Boltzmann coefficient
σ_{\parallel}	Stress parallel to the weld
$\sigma_{\perp}^{^{''}}$	Stress perpendicular to the weld
σ_y	Yield stress
θ	Rotation angle for global to local coordinate system
Latin symbols	
2c	Crack width
\dot{Q}	Heat flux
\boldsymbol{A}	Area
\boldsymbol{A}	Paris Law constant
a	Crack depth
a_r , a_f , b , c , f_r , f_p	Goldak semi-elliptical heat source parameters
C_n , n	Residual stress distribution fit parameters
c_p	Specific heat
E	Young's modulus
е	Emissivity coefficient
F_n	Factor for the weight function method
f_w	Factor for finite width
h_c	Convective heat loss coefficient
K	Stress intensity factor
k	Conductivity
K_I	Mode I stress intensity factor
L	Specimen length, defined in welding direction
L	Specimen length
$L_{80\%}, L_{90\%}$	Highly stressed length
M	Factor to incorporate mean stress effect in fatigue crack growth
m M	Paris Law or S–N curve slope Correction factor for comi alliptical curface graphs subject to membrane leading
M_m	Correction factor for semi-elliptical surface cracks subject to membrane loading Magnification factor for the weld geometry
$egin{aligned} M_{km} \ N \end{aligned}$	Number of cycles to fatigue failure
N N	Number of cycles Number of cycles
P	Power input during welding
R	Stress ratio
$R_{ m eff}$	Effective stress ratio
Teff T	Temperature
t	Time
t_w	Web plate thickness
$\stackrel{\iota_w}{V}$	Volume
v	Welding velocity
x, y, z	Global coordinates
x', y', z'	Local coordinates

have been larger than this highly stressed length, but no significant difference is expected. The other sources reported the nominal stress and the full specimen length. The figure shows a decreasing fatigue strength with specimen length, which can be attributed to (i) differences in residual stress, (ii) a plane stress condition at the specimen edges (relevant only for extremely short welds

Subscripts (multiple used)

 $\begin{array}{ccc} \text{max} & \text{At maximum load} \\ \text{min} & \text{At minimum load} \\ \text{0} & \text{At weld start} \end{array}$

a For the deepest point of the crack

For the surface point of the crack

load For the applied load ref Of the reference length

Abbreviations

FE Finite Element

HAZ Heat affected zone

LC Load carrying

NLC Non-load carrying

RS Residual stress due to welding

WP Weld pass

and not for normal fatigue test specimens), and/or (iii) statistical aspects related to the weakest link process, for which theories of highly stressed length or volume are available [5–8]. Of these three, the difference in residual stress remains the source of the largest uncertainty. The process of cutting the specimen redistributes the residual stresses since a lower level of constraint allows for more deformation and, therefore, lower residual stress [9–11]. For establishing S–N curves, it is essential that the specimens are of sufficient length such, that their fatigue life can be (conservatively) used for general purposes. The question arises what length is acceptable? Liang et al. [12] show experimentally that the residual stress at the plate surface mainly relaxes in the longitudinal direction (weld direction) after cutting a 160 mm long cruciform joint to smaller lengths. Similar conclusions follow from studies of Altenkirch et al. [13] and Jiang et al. [14] for a bead-on-plate and multi-pass butt weld, respectively, although they do not show the residual stress distribution along the complete weld toe line. As a follow-up to et al. [12], Zhan et al. [15] apply numerical modelling of the welding process, with significant simplifications, to determine the stress intensity factors of a crack due to the residual stress field. Zhan et al. [15] show a more distinct decrease of residual stresses perpendicular to the weld toe. They also show that the stress intensity factor of a crack in an as-welded specimen is larger than in a specimen cut from a larger welded plate assembly to the same length.

Currently, in linear elastic fracture mechanics calculations, the residual stress field can be included using prescribed residual stress fields by BS 7910 [16], but these can be conservative [17]. Residual stresses can be estimated for a given geometry by means of measurements or simulations. The formation of residual stresses during welding is complex and depends on a large number of variables, such as geometry, welding method, heat input, welding velocity, welding sequence, material properties, and constraints [11]. Measuring residual stresses is cumbersome, especially at locations of stress concentrations, such as a weld toe [18]. Another disadvantage of measuring residual stresses is that widely used non-destructive techniques, such as X-ray diffraction, measure residual stresses to a maximum of 30 μ m below the surface (with electro-polishing allowing measurements up to 2 mm) [19,20]. Therefore, attempts to determine residual stresses using numerical models are presented in the literature. Options for simulating the welding process for the determination of residual stresses and deformations using the finite element (FE) method presented in the literature can be divided into two methods: (i) transient non-linear thermo-mechanical analysis, and (ii) elastic inherent strain method [21]. The latter avoids the thermal analysis and is therefore less computationally expensive, but it is less accurate than the first modelling technique regarding residual stress, and is therefore mostly used in welding deformation analyses [22].

In this study, a transient thermo-mechanical FE model simulating the welding process of a cruciform joint is used to assess the residual stresses at the weld toe of a load carrying cruciform joint and to determine the redistribution of the residual stress after cutting the specimen into smaller lengths. The cutting length is varied, providing insight into the relationship between specimen length and residual stress. The width and height of the specimen are kept constant. Linear elastic fracture mechanics is used to estimate the effect of the resulting residual stress on the fatigue resistance of a fatigue crack at the weld toe. The resulting relationship between specimen width and fatigue resistance is compared to the results of fatigue tests, as in Fig. 1. Section 2 discusses the FE modelling and fatigue life assessment methodology. Section 3 presents the effect of specimen length on the residual stress level and fatigue life. Discussion and conclusions are given in Section 4 and Section 5, respectively.

2. Methods

This section presents the FE modelling method for determining the welding-induced residual stresses and the fracture mechanics-based method for assessing the fatigue life, including the residual stress level for a fatigue crack at the weld toe.

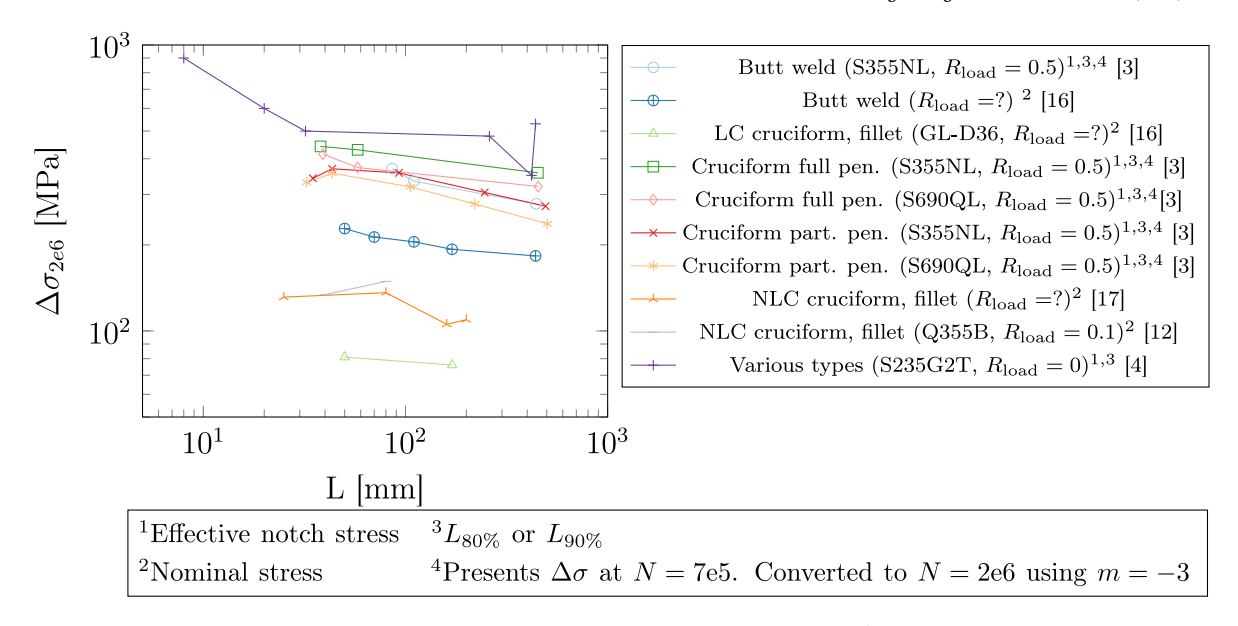


Fig. 1. Effect of specimen length on fatigue strength given in stress range at $N = 2 \cdot 10^6$ cycles; sources [3,4,12,23,24].

2.1. Finite element modelling

Fig. 2 presents the geometry of the cruciform joint that is the subject of this study. The numbers and symbols in the figure represent the sequence and direction of the weld passes. The arrows below the figure indicate the direction of the transverse stress in the loading direction in the flange σ_{\perp} , which is perpendicular to the weld direction, and the longitudinal stress σ_{\parallel} , which is parallel to the weld direction. The transverse residual stress in the *y*-direction is not of interest for this study because the loading direction aligns with the *z*-direction, creating a fatigue crack with its plane perpendicular to the *z*-direction. In the remainder of the paper, the transverse residual stress in the *z*-direction is referred to as transverse residual stress. The specimen length is defined in the longitudinal direction. The plates are cut in the yz-plane to obtain smaller specimen lengths, as discussed in Section 2.1.2. The plates are supported out-of-plane during the welding process simulation. After welding, the plates are unclamped, and only boundary conditions to avoid rigid body motion are included. Two variations in geometry are regarded: (i) with a weld seam, and (ii) without a weld seam. The former corresponds to a fillet weld, whereas the latter corresponds to a full penetration weld. However, only the difference in structural behaviour is regarded; any thermal differences are neglected. The heat input of a fillet weld is considered in this study. The heat input of a full penetration weld will be larger.

3D FE simulations are performed with Abaqus FEA version 2024. Two separate models are constructed: one for the thermal analysis and the other for the mechanical analysis. The models have identical meshes, enabling direct imposition of the nodal temperature from the thermal to the mechanical model without interpolation. In both analyses, 8-node linear brick elements are used; type DC3D8 for diffusive heat transfer in the thermal analysis, and type C3D8 for stress/displacement in the mechanical analysis. Fig. 3 presents the mesh applied in the FE model. The minimum mesh size in the heat-affected zone is approximately 1.75 mm, and it increases towards the edge of the plates in the y- and z-directions to 10 mm. A multi-part mesh refinement is used, where the nodes at the interface between the parts are tied, with correct representation of the displacement field as verified in [25]. The mesh sizes are based on mesh sensitivity studies conducted in [17,26-28]. The total number of elements is 82380. Each weld pass is divided into 60 blocks, each 10 mm long. The weld is deposited by subsequently activating a single block, utilizing the element "death & birth" technique in the thermal analysis through the Model Change option in Abaqus, and the "quiet element" technique in the mechanical analysis, by setting the stiffness of deactivated blocks to $5\cdot 10^{-4}$ times the Young's modulus at room temperature. In both simulations, it is assumed that the base plates and filler material have the same material properties. The red numbers and symbols in Fig. 2 indicate the weld pass sequence and the weld direction used in the study. The bottom web plate is activated in the same manner as the blocks representing the welds, and it is activated together with the first block of the third weld pass. This method prevents heat transfer into undeposited elements, allows heat loss through elements at the borders of only deposited elements, and reduces numerical difficulties in the mechanical analysis due to the initial deformations of undeposited elements. In the mechanical analysis, tack welds are simulated by activating the outer two blocks of 10mm in length of each weld pass before the remaining weld pass is deposited.

2.1.1. Thermal analysis

The three-dimensional governing differential equation for transient heat transfer is:

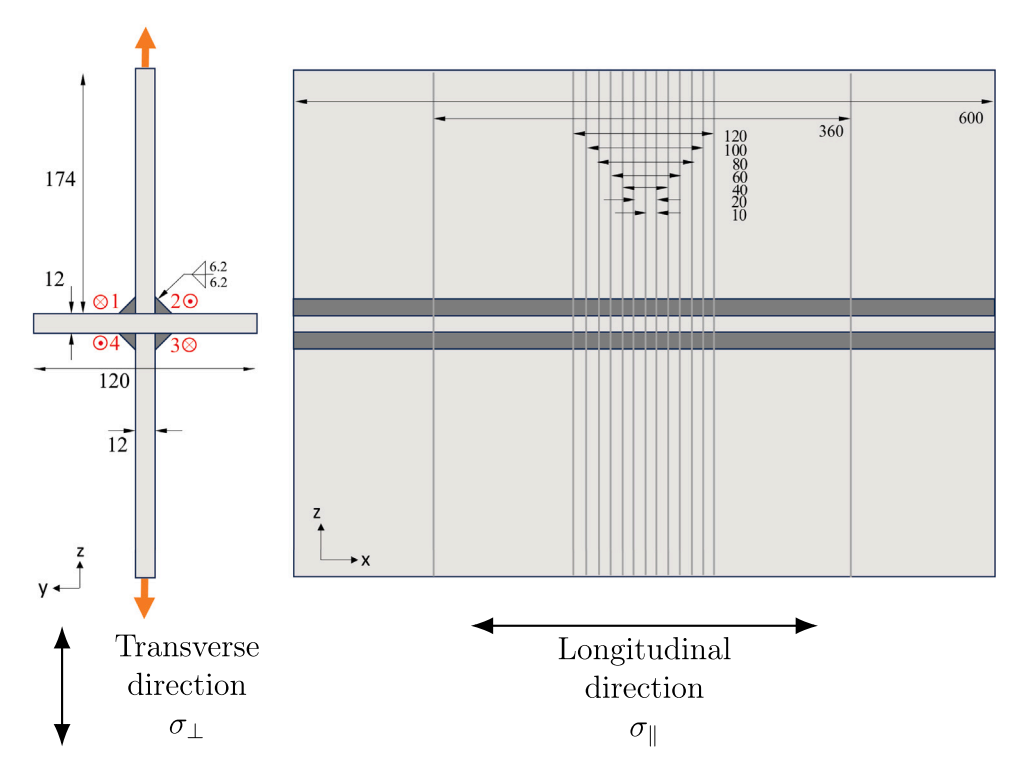


Fig. 2. Cruciform joint geometry. All values are in mm. The red numbers and symbols indicate the welding sequence and direction, respectively. The orange arrows indicate the direction of fatigue loading.

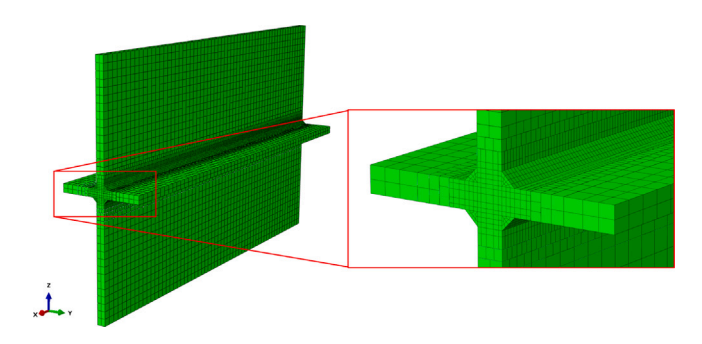


Fig. 3. Overview of mesh.

$$c_p(T)V\rho\frac{\partial T}{\partial t} = k(T)V\left(\frac{\partial^2 T}{\partial x^2} + \frac{\partial^2 T}{\partial x^2} + \frac{\partial^2 T}{\partial x^2}\right) + \dot{Q}_{in}(x, y, z) + \dot{Q}_c(T) + \dot{Q}_r(T) \tag{1}$$

where $c_p(T)$ equals the temperature-dependent specific heat, V is the material volume, ρ is the density, taken as a constant of 7850 kg/m³, T(x,y,z) is the temperature at coordinate x, y, and z, t equals time, k(T) is the temperature-dependent conductivity, $\dot{Q}_{in}(x,y,z)$ is the heat flux into the material by welding, $\dot{Q}_c(T)$ is the heat loss due to convection, and $\dot{Q}_r(T)$ is the heat loss due to radiation. The convective and radiative heat fluxes form the boundary conditions of Eq. (1):

$$\dot{Q}_c(T) = -h_c A \left(T - T_{RT} \right) \tag{2}$$

$$\dot{Q}_r(T) = -e\sigma_R A \left(T^4 - T_{PT}^A \right) \tag{3}$$

where h_c is the convective heat loss coefficient, taken as $h_c = 20 \text{ Wm}^{-2}\text{K}^{-1}$, A equals the area, T_{RT} is the room temperature, taken as 25 °C, e is the emissivity coefficient, taken as 0.9, and the Stefan–Boltzmann coefficient equals $\sigma_B = 5.67 \cdot 10^{-8} \text{ Wm}^{-2}\text{K}^{-4}$.

The mechanical analysis indicates that the gap is decimated during welding, as will be explained in Section 3.2. This enables heat transfer by conduction. In the thermal analysis, the gap between the web and flange plate is therefore neglected, assuming that heat transfer between the flange and web plates occurs entirely through conduction. The heat transfer through convection and radiation is small compared to conduction and is therefore neglected.

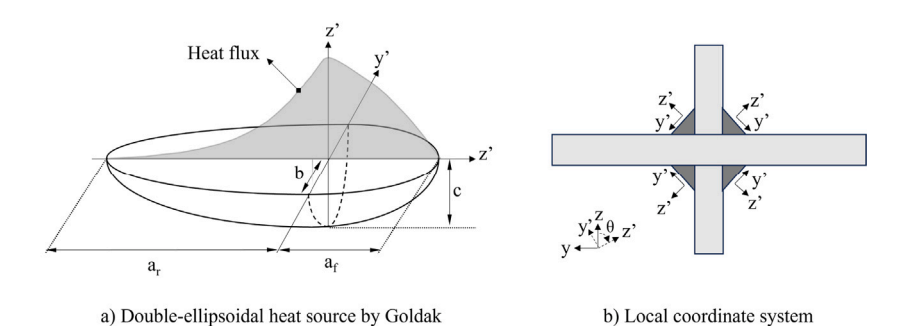


Fig. 4. Goldak heat source model.

Table 1 Welding simulation input parameters.

v [mm/s]	P [W]	η [-]	a_f [mm]	a_r [mm]	b [mm]	c [mm]
1.33	2800	85%	4.5	12	4.5	4.5

Most detailed transient non-linear thermo-mechanical FE analyses in the literature use the double ellipsoidal heat source model of Goldak [29] for simulating the heat input from the arc welding process [30–36]. The significant computational time of this method can be reduced by using a sub-modelling approach [37], a combination of 2D and 3D elements [38], a combination of linear and non-linear material properties [28], or a constant initial temperature or heat flux per weld pass instead of a moving heat source [31,39,40]. In this study, the moving double-ellipsoidal heat source proposed for arc welding by Goldak is applied. Because of the multi-part mesh, the total computational time was acceptable. The volumetric heat flux is imposed on the model using the Abaqus subroutine DFLUX and is determined using:

$$\dot{Q}_{in}(x,y,z) = \begin{cases} \frac{6\sqrt{3}f_r\eta PV}{a_rbc\pi\sqrt{\pi}} \exp\left(-3\left(\frac{x'(x)^2}{a_r^2} + \frac{y'(y,z)^2}{b^2} + \frac{z'(y,z)^2}{c^2}\right)\right) & \text{if } x'(x) < 0, \\ \frac{6\sqrt{3}f_f\eta PV}{a_fbc\pi\sqrt{\pi}} \exp\left(-3\left(\frac{x'(x)^2}{a_f^2} + \frac{y'(y,z)^2}{b^2} + \frac{z'(y,z)^2}{c^2}\right)\right) & \text{otherwise.} \end{cases}$$
(4)

where a_r , a_f , b, and c are Goldak parameters defining the double ellipsoid in mm (see Fig. 4), η is the arc efficiency, P is the power input, and t_{n0} is the start time of the nth weld pass. The input values are presented in Table 1. The welding velocity v and power P are determined by consulting a construction company that produced specimens with the exact geometry of Fig. 2. The Goldak parameters a_f , b, and c are taken as equal, similar to other studies [17,31–33,36]. The ratio a_f/a_r ranges between 0.25 and 0.5 in other studies [17,31–33,36] and is taken as the centroid of that range $a_f/a_r = 0.375$ in the current study. Finally, a_f is calibrated by trial such that the depth of the heat-affected zone approximates the weld throat dimension.

A local coordinate system (x', y', z') is created for each weld pass, ensuring that the double-ellipsoidal heat source is applied to the weld surface, see Fig. 4. The local coordinate system is defined as:

$$x' = x - x_0 - vt, y' = (y - y_0)\cos\theta - (z - z_0)\sin\theta, z' = (z - z_0)\cos\theta + (y - y_0)\sin\theta$$
 (5)

where subscript 0 indicates the starting position of the weld pass. The rotation angle θ is defined in Fig. 4b. The front and rear heat apportionment of the heat flux, f_f and f_r respectively, are assumed as in Eq. (6) [41], corresponding to $f_f + f_r = 2.0$ as advised by Goldak et al. [29].

$$f_f = \frac{2a_f}{a_r + a_f},$$

$$f_r = \frac{2a_r}{a_r + a_f}$$
(6)

Table 1 shows the chosen welding parameters. The cooling time after each weld pass is $t_{cool} = 1000$ s. After the last cooling phase, the temperature in the entire model is reset to room temperature.

Fig. 5 presents the temperature dependent thermal conduction and specific heat. The figures show relationships from the literature for steel grade S355 or similar, used for welding simulations. There are clear differences among the various literature sources. The peak in thermal conduction at the melting temperature ($T_{melt} = 1480$ °C) and higher ranges between 100 and 300 W/m°C. This peak is artificial, and it is introduced because of the stir effect caused by the flow of molten weld material, resulting in significantly larger heat transfer. Rikken et al. [30] did not include this peak because they measured this relation

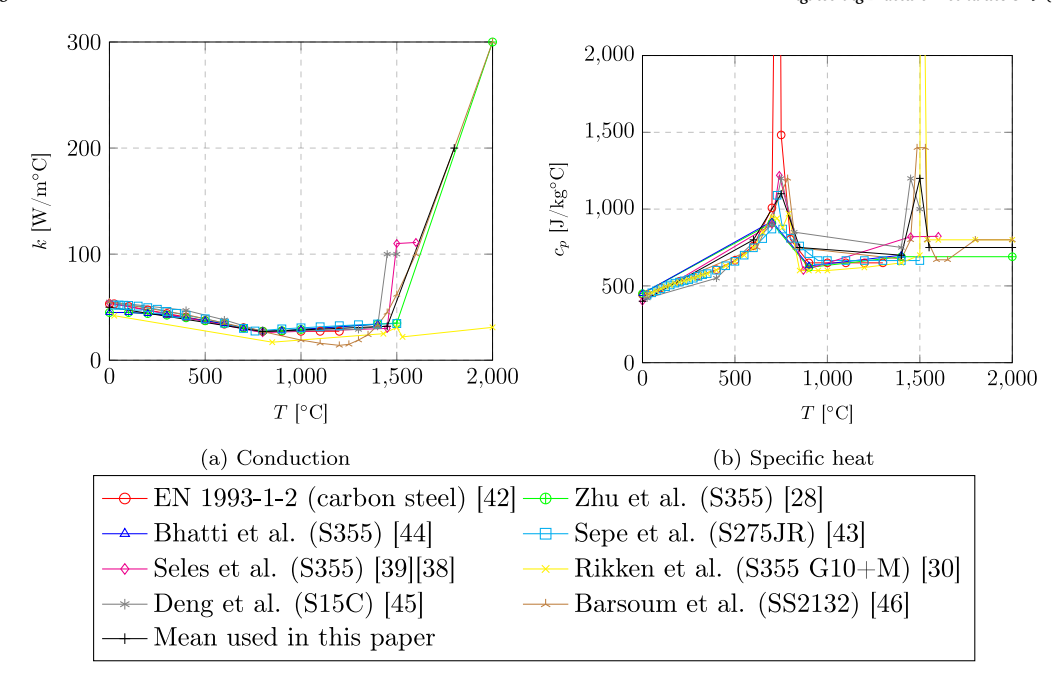


Fig. 5. Time-dependent thermal material properties used for welding simulations in various literature sources for steel grade S355 or similar; sources [28,30,38,39,42–46].

and did not edit the measurements for input into their model. Two peaks are found in the specific heat relationship. The peak at ~ 700 °C corresponds to the austenitic phase transformation and ranges between 900 and 1200 J/kg°C. The relationship according to EN 1993-1-2 [42] is significantly larger (5000 J/kg°C), however, this relation is not provided for this type of FE simulations. The thermal conduction relationship is assumed to be equal for heating and cooling in the FE simulation, whereas, in reality, the material shrinks during the austenitic phase transformation while heated and expands during the austenitic phase transformation while cooled, resulting in a discharge or absorption of energy, respectively. Further, the volume change, and hence the amount of energy at heating and cooling, is different. Some martensite may form during cooling, which also results in a different volume change. Because this peak is used for both heating and cooling, it does not describe the austenitic phase transformation. Justification for this simplification is that it has a negligible effect on the resulting temperature distribution [43]. The peak in the specific heat at T_{melt} is artificially applied because of the latent heat during the solid–liquid and liquid–solid state transformations. This peak ranges between 800 and 4000 J/kg°C. It ensures that the temperature of the material cannot exceed T_{melt} by a significant amount. Sepe et al. [43] have shown that the assumptions of constant values of conduction and specific heat have a negligible effect on the temperature distribution. This demonstrates that the dependency of the two variables on temperature is not important for the aim of the current study. Therefore, a mean relation is estimated from the presented sources and used as input in this study, as indicated by the black curve in Fig. 5.

2.1.2. Mechanical analysis

The mechanical analysis consists of three subsequent steps:

- 1. determination of residual stresses and deformations in the as-welded condition, with the plates supported out of plane at their edges, as shown in Fig. 6;
- 2. all boundary conditions from Step 1 are removed and replaced by fixing a minimum number of nodes to prevent rigid body motions, simulating the unclamping of the specimen, as shown in Fig. 6;
- 3. the specimen length is stepwise reduced to the cutting lengths presented in Fig. 2 by using the "quiet element" technique. The boundary conditions, as in Step 2, to prevent rigid body motions, are applied to the edges of each model at x = -L/2 and x = L/2.

In Step 1 of the mechanical analysis, the temperature field for 15 time-steps per weld block is imported from the thermal analysis. In Steps 2 and 3, the change in the residual stress state due to a change in boundary conditions and geometry is determined. The total strain increment $\Delta \epsilon_{tot}$ generally consists of the following components:

$$\Delta\epsilon_{tot} = \Delta\epsilon_e + \Delta\epsilon_{np} + \Delta\epsilon_{tp} + \Delta\epsilon_{th} + \Delta\epsilon_{vol} + \Delta\epsilon_c \tag{7}$$

where $\Delta\epsilon_e$ equals the elastic mechanical strain increment, $\Delta\epsilon_{np}$ the ordinary plastic strain increment, $\Delta\epsilon_{tp}$ the plastic strain increment due to transformation plasticity, $\Delta\epsilon_{th}$ the thermal strain increment, $\Delta\epsilon_{vol}$ the strain increment due to volume change, and $\Delta\epsilon_c$ the strain increment due to creep.

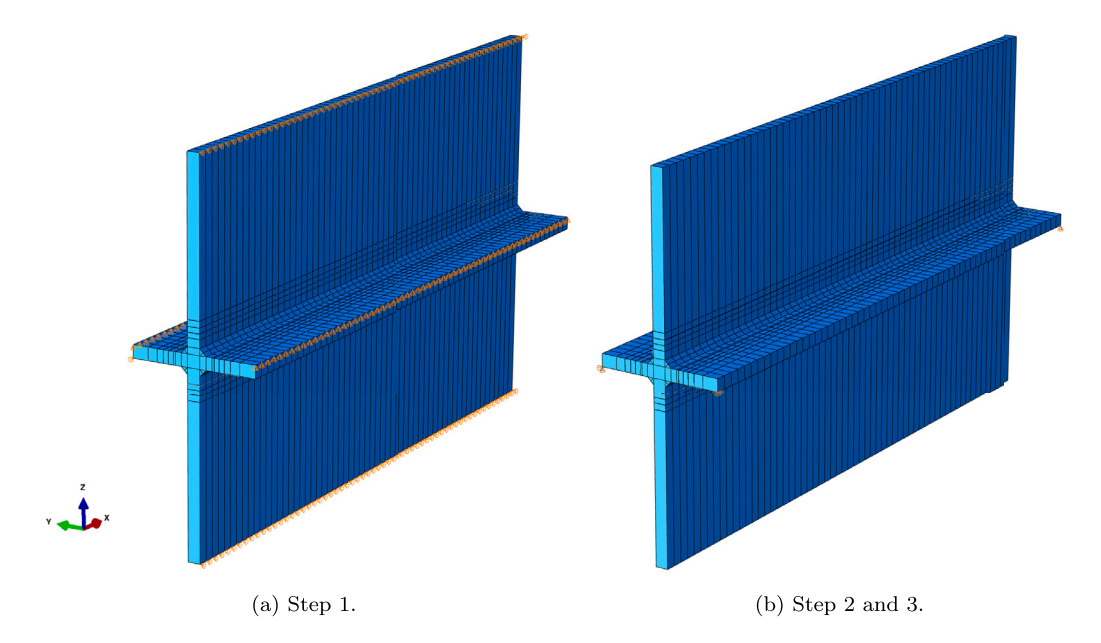


Fig. 6. Mechanical boundary conditions.

During welding, the phase composition close to the weld changes [2]. Phase transformations can change the material properties of steel, result in a change in volume, eliminate the strain history, and under an applied stress, result in transformation plasticity [11]. Therefore, phase transformations can significantly affect the residual stress and deformations [26]. Analytical and empirical equations describing phase transformations can be used in FE models [47,48]. The volume change for all phase transformations is required as input to determine $\Delta\epsilon_{vol}$. $\Delta\epsilon_{tp}$ can be described by the analytical formulae proposed by Inoue, Leblond, and Fischer et al. [49–51]. Again, experimental values are required as input. Phase transformations not only result in $\Delta\epsilon_{tp}$ and $\Delta\epsilon_{vol}$, but also affect the material properties used for calculating $\Delta \epsilon_e$ and $\Delta \epsilon_{np}$. These material properties of all phases, e.g., the stress-strain curve, are difficult to obtain and are not available in the literature for steel grade S355 or similar. According to Goldak and Barsoum [52], phase transformations should be included in welding simulations using FE methods for materials with (i) a high yield strength, (ii) a phase transformation temperature close to room temperature, or (iii) significant volumetric strains due to a phase transformation. Deng [45] performed welding simulations with S15C (0.15 wt% C) and S45C material (0.45 wt% C) and concluded that phase transformations should be included for S45C, but not for S15C. He identified carbon content as the driving force for the effect of phase transformations on residual stresses. This corresponds with the recommendations of Goldak and Barsoum, since S45C has a significantly larger volumetric strain and a lower starting temperature at the martensitic transformation. However, a welding simulation of low carbon S355G10+M structural steel (0.07 wt% C) was conducted by Rikken et al. [30] shows a difference in the residual stress distribution between simulations that include and exclude phase transformations, where the results that include phase transformations show good agreement with measurements. Also, Heinze et al. [26] showed that phase transformations cannot be neglected for S355J2+N steel. On the other hand, Heinze et al. [53] concluded that the effect of transformation plasticity in welding S355J2+N steel is negligible. Suman et al. [54] included transformation plasticity by virtually reducing the yield strength in the martensitic phase and stated that the effect of transformation plasticity in the austenitic phase is negligible. The outcomes of these studies depend on the steel grade and the applied welding parameters. For the constraints in the current study (Fig. 2), phase transformations will also be influential. However, phase transformations are neglected for two reasons: (i) due to the lack of required input data and (ii) because this study aims to provide a qualitative comparison between the residual stresses in specimens of different lengths and their relative reduction or extension in fatigue life. Creep is not modelled explicitly because time-dependent material behaviour only occurs at very high temperatures, at which the stiffness is very low. Therefore, Eq. (7) is simplified to:

$$\Delta\epsilon_{tot} = \Delta\epsilon_e + \Delta\epsilon_{np} + \Delta\epsilon_{th} \tag{8}$$

Fig. 7 presents the temperature-dependent Young's modulus E, yield stress σ_y , and linear expansion coefficient α used for welding simulations in various literature sources for steel grade S355 or similar. Sepe et al. [43] show that variations in these parameters can significantly influence the residual stresses and deformations. This study adopts the stress–strain relation as defined for carbon steel in EN 1993-1-2 [42] because the Young's modulus and yield stress are in good agreement with the other sources. The non-linear stress–strain relation is applied in the FE models, using the von Mises yield criterion and considering isotropic strain hardening. The latter is applied because [55] shows that residual stresses from a welding simulation with an isotropic hardening model are in better agreement with experimental results compared to combined or kinematic hardening models. In some studies, an annealing temperature just below $T_{\rm melt}$ is set in the welding simulation, at which the strain history is reset [11,32,56]. This is not applied in

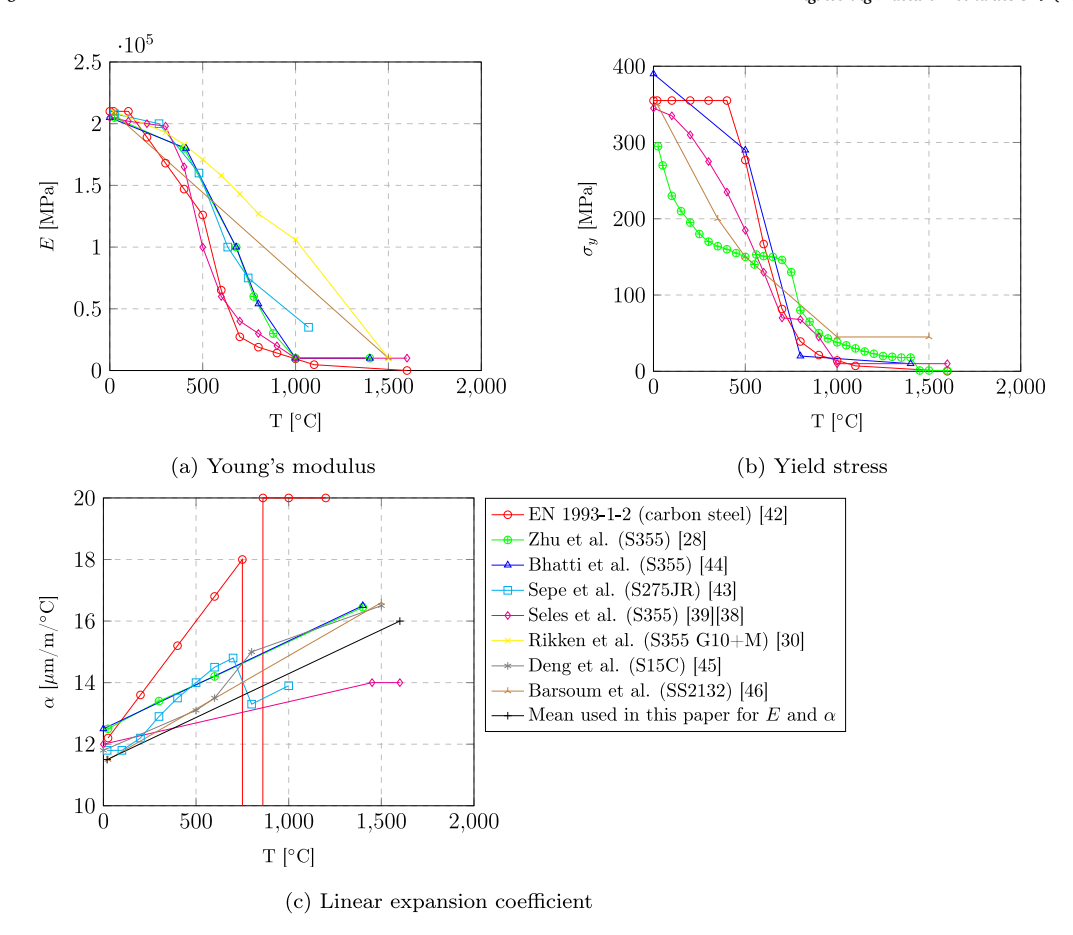


Fig. 7. Time-dependent mechanical material properties used for welding simulations in various literature sources for steel grade S355 or similar; sources [28,30,38,39,42–46].

this study since the Young's modulus and yield stress are negligibly low at this temperature. Hence, it will have a negligible effect on the residual stress.

For the linear expansion coefficient α , used for determining $\Delta\epsilon_{th}$, the relationship as given in EN 1993-1-2 [42] does not agree with the other data sources. A linear mean relation is estimated from the other data sources and is used in this study, see the black curve in Fig. 7c.

As explained in Section 2.1, two variations of the mechanical analysis are considered with the same thermal input, namely, one with a weld seam and one without. The weld seam is introduced in the mechanical model by uncoupling two sets of nodes at the interfaces between the flange and web plates, as indicated by the red nodes in Fig. 8. The blue nodes in Fig. 8 indicate the stress read-out points at the weld toes of each weld pass (WP). The stress is not determined exactly at the weld toe, since this is a singular point due to the sharp angle between the weld material and the plate. A stress concentration occurs at this point, which will increase with a decrease in mesh size. The read-out points are located 1.7 mm below the surface, at one element in depth. At this location, the singular point can still have an effect, but it will be significantly smaller.

The cutting process in Step 3 is simulated by deactivating elements near the edges of the assembly to lengths indicated in Fig. 2 using the "quiet element" technique. Any heat input due to the cutting process is neglected. Fig. 9 shows the active and inactive material in several steps of the welding simulation. A user defined parameter is created that gives the elements their status as either active (1) or inactive (0). The figure indicates that the element value may also be 0.5 (green in the figure), which corresponds to an 'intermediate' stiffness, depending on the temperature, as a transition between active and inactive material to enhance numerical stability. These elements are part of the prescribed active material because the inactive material is set to 0 in the time steps. The effect of the transition layer on the stiffness of the complete assembly increases as the specimen length decreases. For the smallest specimen length of L = 10 mm, only five active elements remain in the x-direction, of which two are in the transition layer. This simulation therefore represents a specimen length between L = 10 mm (red and green elements) and L = 6 mm (red elements), but will be shown as L = 10 mm in the results section.

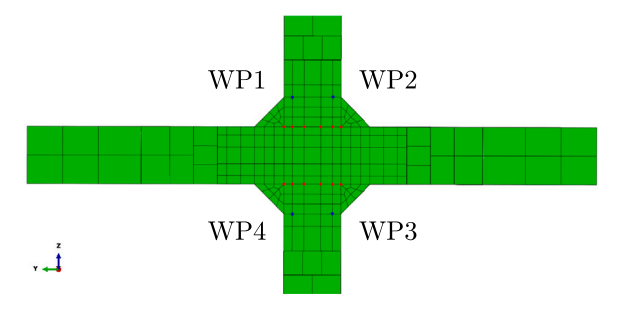


Fig. 8. Specifications of the FE model. The red nodes indicate nodes uncoupled in vertical direction to create seam effect, the blue nodes indicate the stress read-out points.

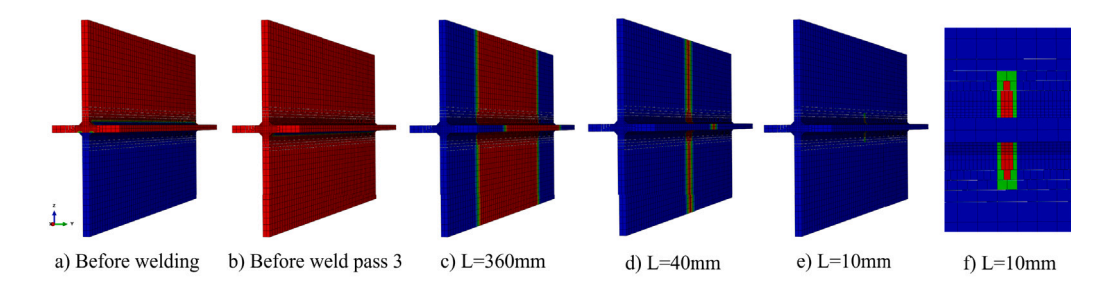


Fig. 9. Active (red) and inactive (blue) material during welding and cutting. Green elements show the transition layer.

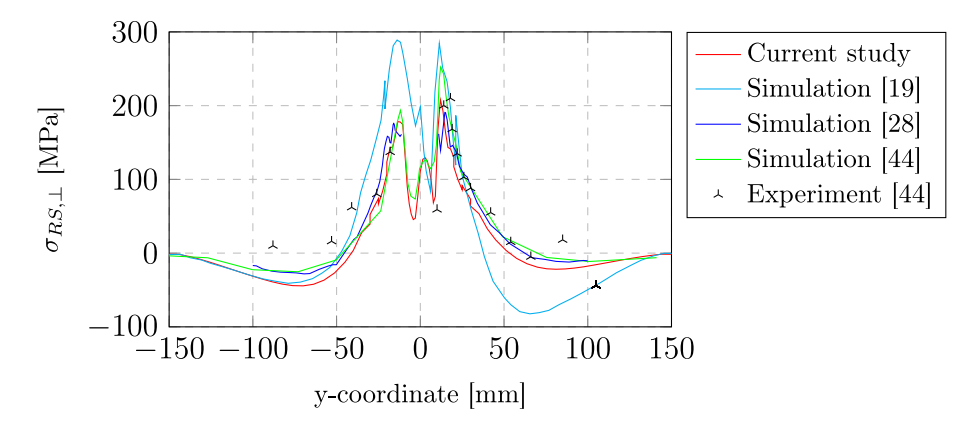


Fig. 10. Transverse residual stress results of the validation study. Stresses are presented at the top surface of the flange plate at the centre of the specimen.

2.1.3. Validation study

The thermal and mechanical FE modelling methodology is validated against experiments in the literature. Fig. 10 shows the transverse residual stress $\sigma_{RS,\perp}$ for a T-joint with fillet welds from measurements and FE analyses. Input parameters of Zhu et al. [28] are applied in the simulation following the methodology in Section 2.1. The figure presents a good comparison between the current study, experiment, and FE simulations from other studies. It should be noted that the angular deflection of the flange plate in Step 2 was overestimated by the current study, similar to Malschaert et al. [17] (personal communication). Since this study is about residual stress, it is not expected to influence the outcome. Another validation is performed on the numerical and experimental study of Seles et al. [39], with similar results.

2.2. Fatigue life assessment

Crack growth simulations for all specimen lengths using linear elastic fracture mechanics are performed based on the British Standard BS7910 [16] to determine the effect of residual stress and residual stress relaxation due to the reduction of the specimen length on fatigue life. The crack growth simulations adopt the theory that the residual stress influences the fatigue life of the

specimen equally to an applied mean stress [1,2]. The mean stress effect is incorporated by a factor M on the stress intensity factor (SIF) range ΔK according to Huang and Moan [57]:

$$\frac{\mathrm{d}a}{\mathrm{d}N} = A \left(M \Delta K \right)^m \tag{9}$$

where a equals the crack depth, N the number of load cycles, and A and m are Paris Law parameters. The Paris Law slope parameter is taken as m = 3. The Paris Law constant A does not affect the outcome of this study. M is determined with

$$M = \begin{cases} (1 - R_{\text{eff}})^{-\beta_1} & \text{if } -5 \le R_{\text{eff}} < 0\\ (1 - R_{\text{eff}})^{-\beta} & \text{if } 0 \le R_{\text{eff}} < 0.5\\ (1.05 - 1.4R_{\text{eff}} + 0.6R_{\text{eff}}^2)^{-\beta} & \text{if } 0.5 \le R_{\text{eff}} < 1 \end{cases}$$

$$(10)$$

where β and β_1 are empirical values, assumed as 0.7 and 0.84, respectively, for steel in [57]. The equation is adapted for the effective stress ratio R_{eff} , incorporating the mean stress effect due to residual stresses. R_{eff} is calculated as proposed by Hensel [58,59]:

$$R_{\text{eff}} = \frac{K_{\text{I,load}}^{\text{min}} + K_{\text{I,RS}}}{K_{\text{I,load}}^{\text{max}} + K_{\text{I,RS}}}$$
(11)

where $K_{I,load}$ equals the Mode I SIF due to the applied loading of the specimen, and $K_{I,RS}$ is the Mode I SIF for the residual stress field. The superscript min and max denote the minimum and maximum values in the load cycle, respectively.

A single crack of semi-elliptical shape is assumed. Various initial crack sizes are adopted in the literature for fatigue life simulations of as-welded details using fracture mechanics. Mean values of the crack depth a_i often used are 0.1mm or 0.1 mm, and the aspect ratio a_i/c_i varies between 1 and 0.4 [60]. The current study uses the upper bound of the mean crack size: $a_i = 0.15$ and $a_i/c_i = 0.4$. In the crack growth simulation, we assume a semi-elliptical-shaped initial crack, with a depth and aspect ratio of $a_i = 0.15$ mm and $a_i/c_i = 0.4$, respectively. The crack is located at the weld toe in the web plate. A coupled crack growth simulation of the deepest point and the surface point of the semi-elliptical crack is applied, with for both points:

$$K_{\text{Lload}} = f_{\nu\nu} M_m M_{km} \sigma \sqrt{\pi a}$$
 (12)

where M_m is the correction factor for semi-elliptical surface cracks subject to membrane loading according to Newman & Raju [61], and M_{km} is the magnification factor for the weld toe geometry according to Bowness & Lee [62]. No differentiation in M_{km} is made between the simulation with a weld seam and that without a weld seam. The factor f_w is to include the effect of the finite length of the specimen according to BS 7910 [16], which has little influence on the results. M_m and M_{km} are different for the deepest and surface points, and both factors are functions of the crack depth and the aspect ratio. The developments of crack depth and aspect ratio follow from the simulation.

Failure is assumed when the crack depth reaches 60% of the plate thickness or the crack length reaches the specimen length (2c=L). The applied load ratio R_{load} should be representative of a fatigue test. Therefore, $R_{load}=0.3$, in agreement with Fig. 1. The applied stress range affects R_{eff} , and is taken as $\Delta\sigma_{load}=80$ MPa, equal to the detail category of the weld toe crack of the specimen geometry according to [42]. It is assumed that the crack initiates in the WP with the largest residual stresses, i.e., WP4 for the model without a weld seam, and WP2 for the model with a weld seam. The location along the weld toe where $\sigma_{RS,\perp}$ is largest at the read-out point (see blue points in Fig. 8) is taken as the residual stress at the initiation location. The location of the initial crack is, however, virtually placed in the centre of the specimen, i.e., at x = 300mm.

The weight function method is applied to determine $K_{I,RS}$ for the deepest and surface points of the crack. Fett et al. [63] developed a method to determine the SIFs for surface cracks in plates under power-shaped stress distributions. For a description of a stress field by a nth-power exponential function with coefficient C_n , Fett et al. [63] provide a table with the geometric function F_n as a function of n, the crack depth over web plate thickness ratio a/t_w , and the crack aspect ratio a/c. Eq. (13) presents the equation for the SIF due to the residual stress field at the deepest point $K_{I,RS,a}$ and the surface point $K_{I,RS,c}$ using the method of Fett et al. [63].

$$K_{\text{I,RS,a}} = \sqrt{a\pi} \sum_{s} C_{n,a} F_{n,a} \left(\frac{a}{t_w}\right)^n \tag{13}$$

$$K_{\rm I,RS,c} = \sqrt{a\pi} \sum_{c} C_{n,c} F_{n,c} (c)^n$$
 (14)

The residual stress perpendicular to the crack surface through the thickness of the flange is of interest for the deepest point of the crack. The residual stress perpendicular to the crack surface along the weld too is of interest for the surface point of the crack. Therefore, a separate fit of the residual stress field is required for the deepest and the surface points of the crack. The transverse residual stress is in the same direction as the applied loading and, therefore, perpendicular to the crack surface. The longitudinal residual stress does not influence the crack behaviour according to linear elastic fracture mechanics and is therefore not included in the analysis. Fits of the residual stress field from the FE simulation are required to obtain the parameters $C_{n,a}$, $C_{n,c}$ and n. To reduce the complexity of the analysis, the centre of the initial fatigue crack is assumed at x = 300 mm with a symmetrical transverse residual stress field centred at the initiation location. The transverse residual stress field from the FE analysis is not necessarily symmetrical, and the location of maximum transverse residual stress at the weld too is often not at x = 300 mm. Therefore, the symmetrical transverse residual stress field is determined by the two steps indicated in Fig. 11:

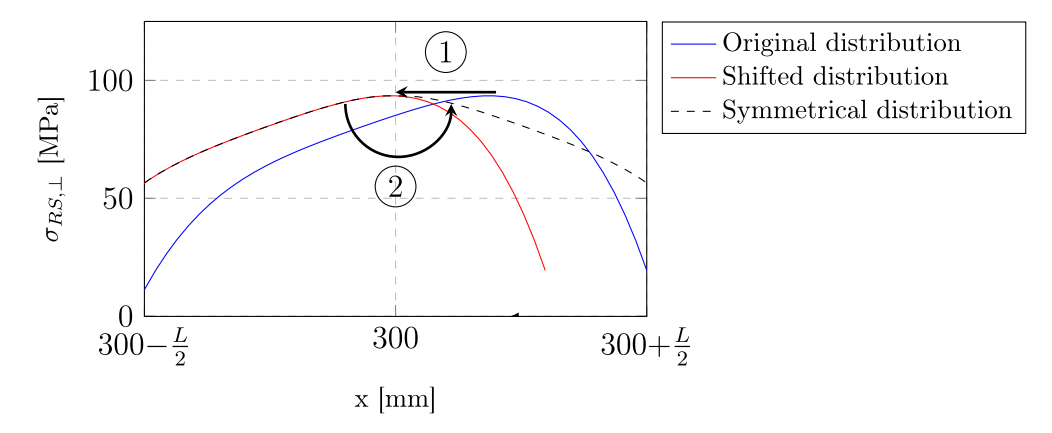
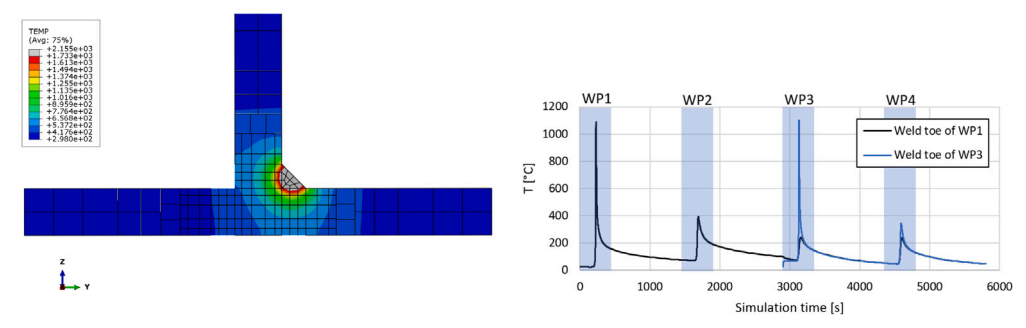


Fig. 11. Example of determination of symmetrical transverse residual stress distribution along the weld toe used for the fit function of Eq. (13).



(a) HAZ during deposition of WP1 in Kelvin. The (b) Temperature development at the weld toe (at grey area shows the molten zone ($T_{\text{melt}} = 1460^{\circ}\text{C}$). the web) of WP1 and WP3 at x=300mm.

Fig. 12. Results of the thermal FE analysis.

- 1. shifting the transverse residual stress field per specimen length such that the largest tensile transverse residual stress is at x = 300 mm
- 2. if the largest transverse residual stress before shifting was at x < 300 mm, the shifted transverse residual stress field within the range $300 \text{ mm} < x < 300 \text{ mm} + \frac{L}{2}$ is considered and mirrored to 300 mm L/2 < x < 300 mm to obtain the symmetrical transverse residual stress field. Vice versa for the case when the largest transverse residual stress before shifting was at x > 300 mm.

A linear equation is fitted through the transverse residual through-thickness stress distribution at x = 300 mm. A polynomial is fitted through the transverse residual stress field along the weld toe (read-out point) for the surface points of the crack for most specimen lengths. The order of the polynomial depends on the shape of the distribution. The nodes at the surface points (weld toe) are not included in the fits because of singularity.

The interaction between a crack and the edge of the plate in determining K_I is neglected by shifting and symmetrizing the residual stress distribution around the centre of the specimen, which is unconservative. Symmetrizing the residual stress distribution using the side with the largest residual stresses is conservative. These effects are only relevant for relatively large fatigue cracks, which are rapidly propagating and therefore comprise only a small part of the fatigue life. Because these effects work in the opposite direction, and their individual contributions are marginal, the combined effect on the fatigue life is deemed negligible.

3. Results

This section presents the temperature and residual stress distribution resulting from the FE analyses discussed in Section 2.1, and thereafter, the results of the fatigue life analyses discussed in Section 2.2.

3.1. Temperature distribution during welding

Fig. 12 shows the resulting heat affected zone (HAZ) of WP1 and the temperature development in the cruciform joint of study at the weld toe of the web plate of WP1 and WP3. The figure shows that the melting temperature was reached in the deposited material. The maximum temperature at the weld toe was close to the melting temperature. The maximum temperature in the weld

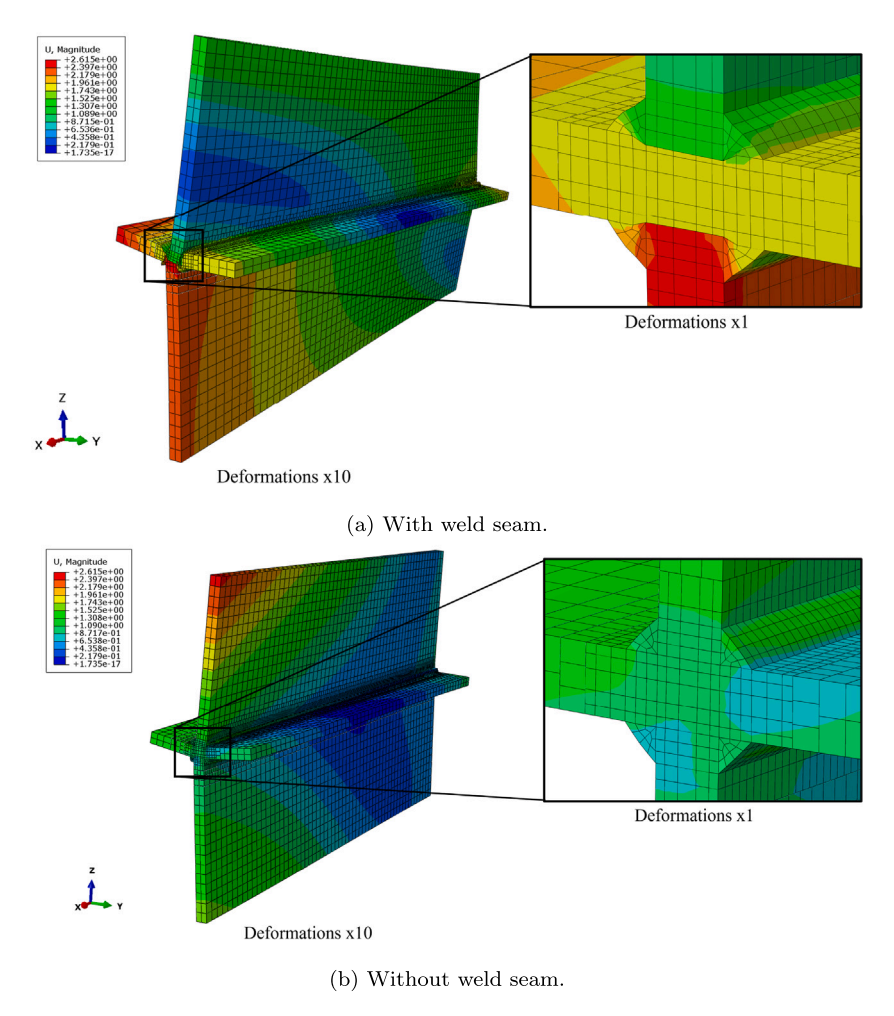


Fig. 13. As-welded deformations after unclamping.

after a cooling step equals 105 °C, which is well below the interpass temperature for this material type. The temperature of the material at the end of the final cooling phase approaches room temperature, demonstrating that a sufficient cooling time has been chosen.

3.2. Residual stress distribution after welding

Fig. 13 shows the deformations of the cruciform joint after Step 2, i.e., in as-welded condition after unclamping. The figure shows significant differences between the simulations with and without the weld seam. The simulation with the weld seam shows a vertical displacement towards the flange plate of both web plates, which is due to the shrinkage of the weld material. Because no contact surface was present, the elements of the web plates moved into the elements of the flange plate. In reality, this is not possible, and it would mean that any existing gap between the plates is reduced or closed. Fig. 13b shows that neglecting the weld seam results in smaller deformations around the weld and primarily a rotation of the web plates around the x-axis.

Fig. 14 presents the transverse residual stresses in the *z*-direction of a cross-section in the center of the assembly (x=300 mm). This stress direction equals the loading direction of the test specimen and is therefore of interest for the fatigue life of the specimen. The vertical displacement of the web plates results in a significant stress concentration at the outer edges of the weld seam, as is clearly visible in the figure. The stresses at the weld root are therefore mesh-dependent and unreliable. Compressive residual stresses are present in the center of the plates, and larger tensile stresses are observed at the surface in the simulation without the seam compared to the simulation with the seam. Most residual stresses relax after unclamping.

Fig. 15 presents the residual stresses at the weld toe (see the read-out points in Fig. 8) over the entire length of the assembly for all weld passes, after unclamping. A small sinusoidal noise is found in the residual stress along the weld toe line because of the activation of blocks of elements during the welding phase. The variations are, however, small. The figure shows a larger difference between the weld passes for the transverse residual stress than for the longitudinal residual stress, which corresponds to the numerical study

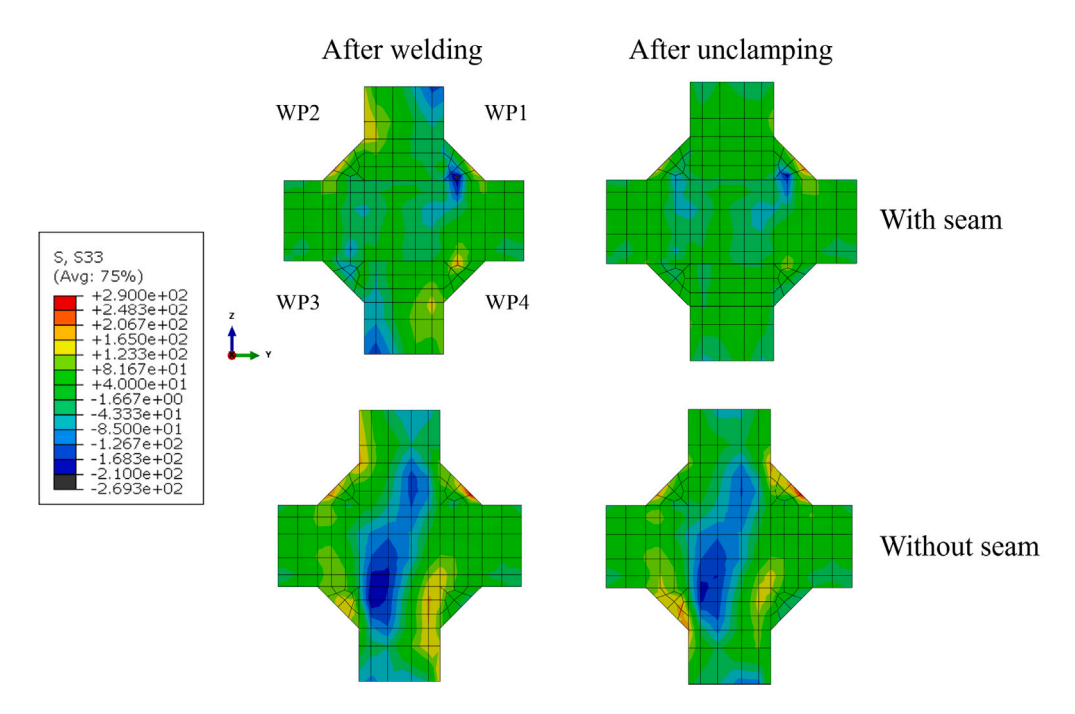


Fig. 14. Transverse residual stresses in z-direction of a cross-section at x=300 mm.

of Fu et al. [32]. The longitudinal residual stress is larger than the transverse residual stress, and it is completely in tension at the weld toe. In contrast, the transverse residual stress at the outer x-coordinate is negative, which corresponds to measurements [12]. The transverse residual stress for different weld passes shows that the welding sequence and direction have a significant influence. The bending stress is larger in the bottom web plate than in the top plate because the degree of constraint is greater after the bottom web plate is welded. The maximum transverse residual stresses at the weld toe are similar in the simulation with and without the weld seam, but the maxima are located in different weld passes. The stress reduces more gradually at the edges for the model with the weld seam.

3.3. Effect of the specimen length on residual stress

Fig. 16 presents the distribution of the transverse residual stress in the z-direction $\sigma_{RS,\perp}$ and the longitudinal residual stress $\sigma_{RS,\parallel}$ along the weld toe of WP2 and WP4 for the geometry with and without the seam, respectively, which have the largest transverse residual stresses. The figure shows that the distribution of the transverse residual stress for the model with the seam is asymmetrical, in contradiction to the model without the seam and the longitudinal residual stress. The figure shows that the residual stress redistribution, in some cases, results in an increase in transverse residual stress at the centre of the specimen (i.e., at x = 300 mm). The subfigures show that the welding induced residual stress decreases with specimen length. This is due to the reduced stiffness of the assembly, which relaxes the residual stresses. Fig. 17 presents the maximum transverse and longitudinal residual stresses along the weld toe of each weld pass for several specimen lengths. Residual stress relaxation is larger and shows a more constant relaxation with specimen length in the longitudinal direction compared to the transverse direction. The difference in transverse residual stress between specimen lengths L = 360 mm and L = 100 mm is negligible for most weld passes in the model with the weld seam. The transverse residual stress is largest at L = 60 mm in the model without the weld seam.

3.4. Effect of the specimen length on the fatigue life

Three variations of residual stress effects are considered: (i) with residual stresses from the FE model with weld seam, (ii) with residual stresses from the FE model with weld seam, and (iii) without any residual stress effects.

Table 2 presents the fit parameter $C_{n,a}$ for the through-thickness transverse stress distribution. Table 3 presents the fit parameter $C_{n,c}$ for the transverse stress distribution along the weld toe. The fit parameters are used to determine the Mode I SIF for residual stress K_{LRS} using Eq. (13).

Fig. 18 presents the effective stress ratio averaged over the fatigue lifetime per specimen length. The figure shows that $R_{\rm eff}$, and therefore M, is almost independent of specimen length for 40 mm< L < 600 mm for the residual stress field without seam. For the residual stress field with seam, $R_{\rm eff}$ gradually increases with specimen length. For short specimens of L < 40 mm, $R_{\rm eff}$ decreases significantly.

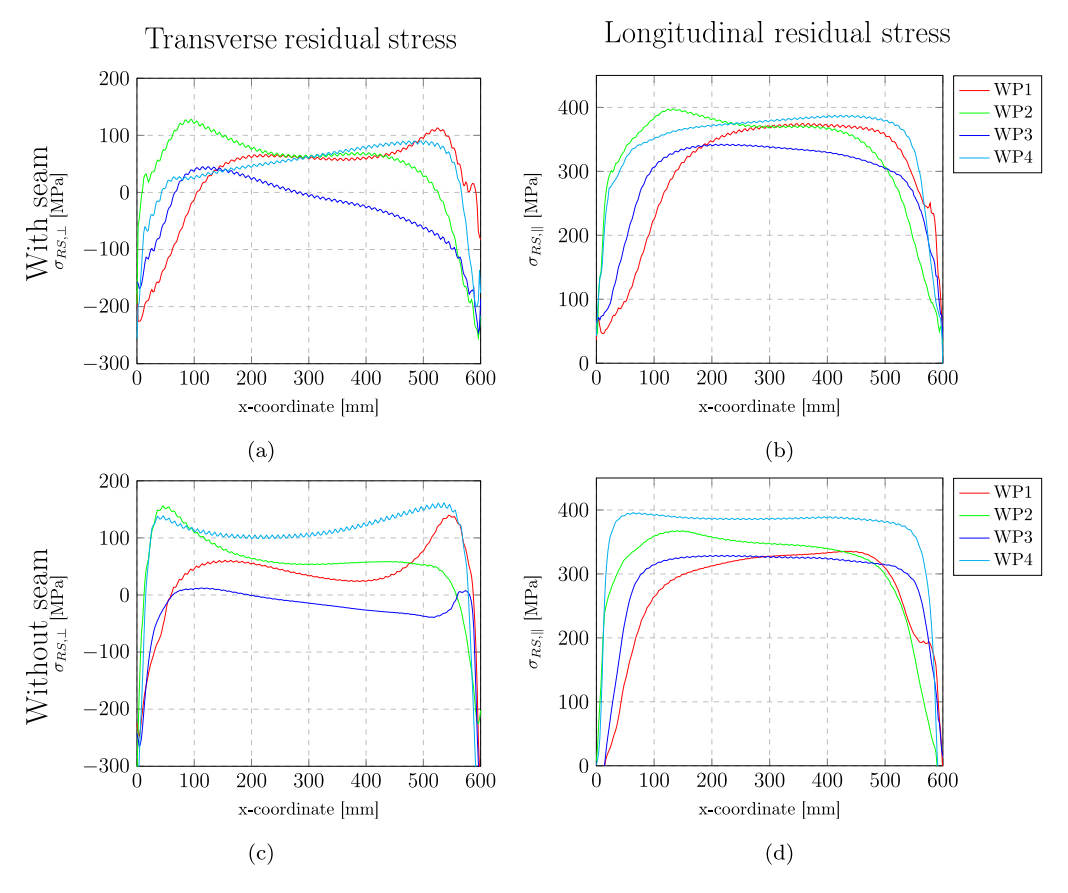


Fig. 15. Residual stress at the weld toe after welding and unclamping in all weld passes.

Table 2 Fit parameter $C_{n,a}$ of through thickness transverse residual stress.

L [mm]	With se	am (WP2)	Without seam (WP4)		
	$C_{0,a}$	$C_{1,a}$	$C_{0,a}$	$C_{1,a}$	
600	136.5	-213.4	166.2	-302.9	
360	105.2	-155.7	140.5	-250.7	
120	88.5	-87.7	147.9	-210.5	
100	83.8	-70.7	153.8	-212.4	
80	84.0	-81.8	159.4	-216.1	
60	74.0	-56.5	162.0	-222.4	
40	72.1	-62.1	155.7	-232.4	
20	61.5	-49.1	129.1	-223.7	
10	8.7	-21.1	23.8	-60.4	

Using the Paris equation slope parameter m=3, the fatigue life is determined relative to the life of a specimen with a reference length of $L_{\rm ref}=100$ mm through crack growth simulation. Fig. 19 presents a comparison between the fatigue strength from experimental data of Fig. 1 and the results of this study. Where no data point of a data series from Fig. 1 was available for L=100 mm, a linear fit through the data set was made to estimate the experimental fatigue strength at L=100 mm.

The black line in the figure shows that a small specimen length results in a slightly lower fatigue strength than for the reference length if residual stresses are ignored because the failure criterion 2c = L is reached. The opposite trend follows if residual stresses are considered. Because of a reduction in residual stresses due to cutting, the fatigue strength increases with a decrease in specimen length. This effect appears larger for the residual stress field from the FE model with the seam than without the seam. The results are in reasonable agreement with the experimental results from the literature, especially for lengths L < 100 mm. For specimen lengths of L > 100 mm, the reduction of fatigue strength is small compared to most literature. This could imply that statistical aspects are more important for weldments with lengths L > 100 mm.

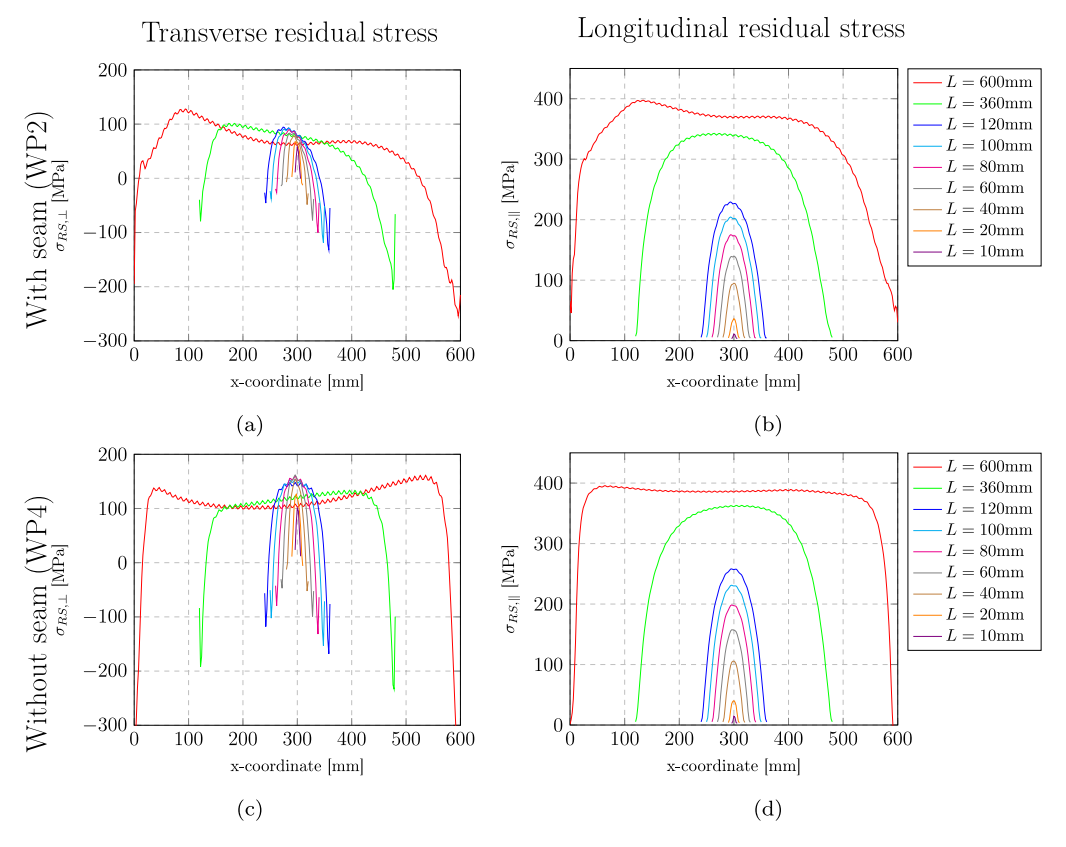


Fig. 16. Residual stress at the weld toe of the weld pass with the maximum transverse residual stress.

Table 3 Fit parameter $C_{n,c}$ of transverse residual stress along the weld toe.

L [mm]		With seam (WP2)					
	$C_{0,c}$	$C_{1,c}$	$C_{2,c}$	$C_{3,c}$	$C_{4,c}$	$C_{5,c}$	
600	127.1	-0.50	0	0	0	0	
360	100.9	-0.20	0	0	0	0	
120	93.7	-0.17	-0.04	1.7E-03	-3.1E-05	1.5E-07	
100	91.5	-0.58	-0.04	1.8E-03	-3.6E-05	1.1E-07	
80	89.9	-0.13	-0.09	4.2E-03	-8.5E-05	3.2E-07	
60	80.3	-1.20	-0.04	3.8E-03	-2.1E-04	1.2E-06	
40	77.9	-0.60	-0.25	1.6E-02	-2.9E-04	-1.2E-05	
20	65.7	3.82	-1.04	2.4E-02	0	0	
10	54.5	-0.38	-2.36	1.4E-01	0	0	
		Without seam (WP4)					
600	159.4	-0.24	0	0	0	0	
360	131.1	-0.11	0	0	0	0	
120	142.7	-0.02	0.01	7.9E-05	-2.6E-05	6.0E - 08	
100	151.6	0.03	-0.01	7.0E-05	-4.4E-05	1.9E-07	
80	159.3	0.24	-0.06	-8.2E-05	-7.8E-05	6.9E-07	
60	162.2	0.83	-0.17	-1.0E-03	-1.5E-04	3.3E-06	
40	152.3	2.26	-0.42	-4.6E-03	-4.5E-04	2.5E-05	
20	127.0	1.76	-1.40	1.3E-02	-7.0E-04	1.4E-04	
10	100.6	6.42	-4.22	-2.4E-01	2.5E-02	5.6E-03	

4. Discussion

Simplifications and assumptions are applied in the complex welding process that involves many influencing parameters. In a benchmark study, Caprace et al. [64] find a difference in the residual stress of up to 20% due to different modelling choices. Studies in the literature often show significant discrepancies between numerical results and experimental data. This is partly attributed to the large uncertainty in welding simulations, but also to the uncertainty in residual stress measurements and the welding process.

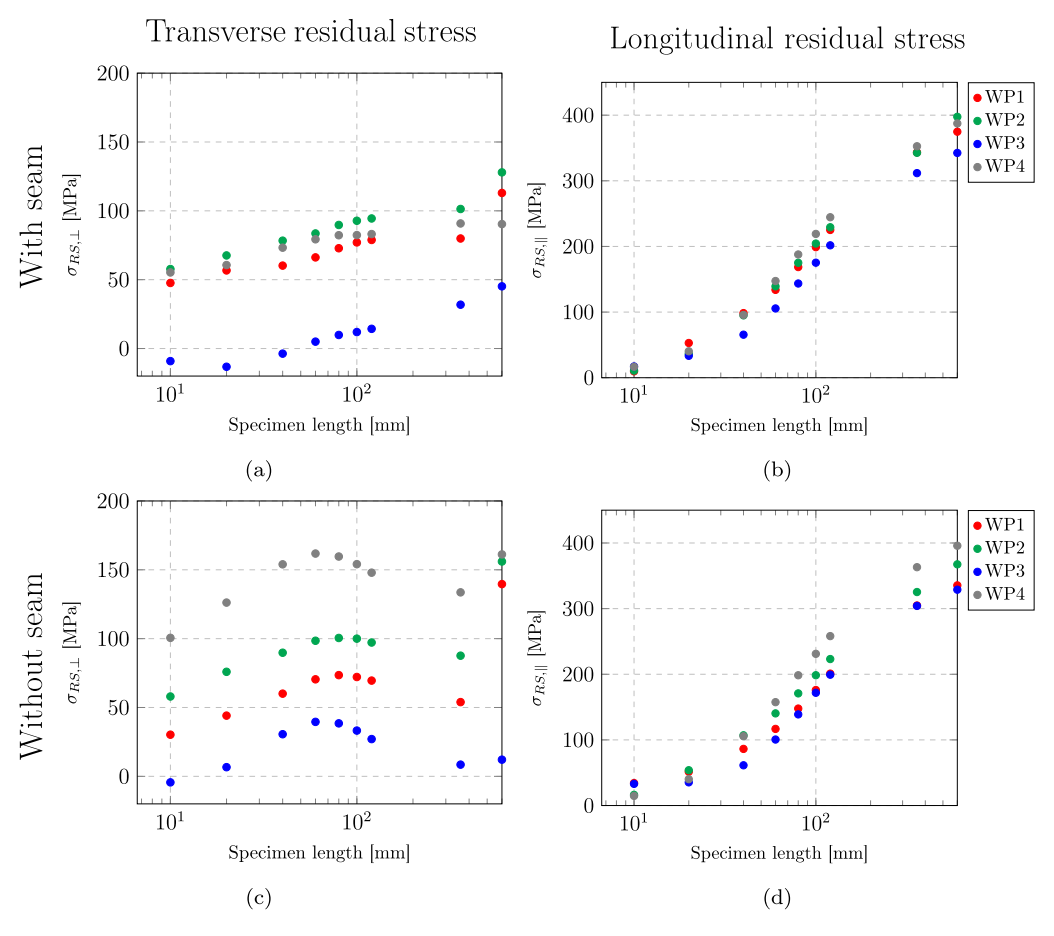


Fig. 17. Maximum residual stresses at the weld toe per weld pass and specimen cutting length at WP2 for the models with seam, and at WP4 for the models without seam.

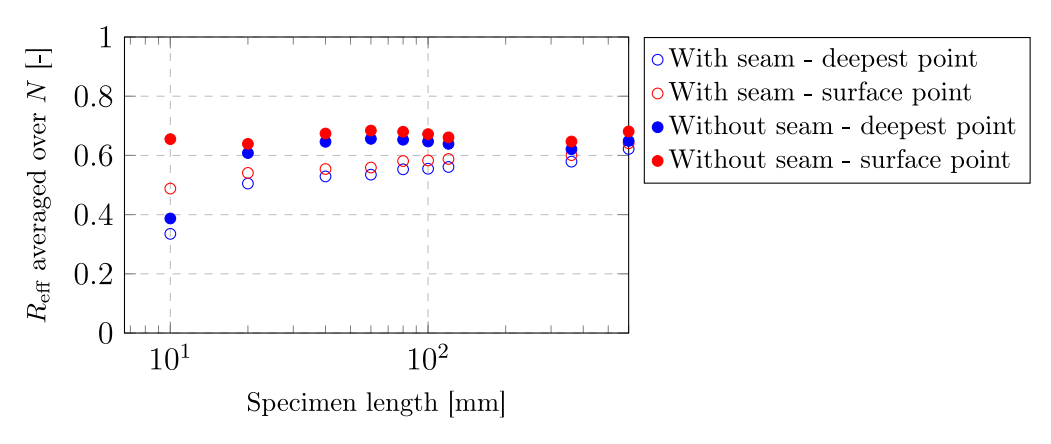


Fig. 18. Effective stress ratio over fatigue life per specimen length.

All physical phenomena involving the welding process are significantly simplified in numerical welding simulations. E.g., phase transitions are often ignored, which can influence the residual stress field [45]. Parameters such as those used for the Goldak double-ellipsoidal heat source model need to be calibrated with measurements to obtain the correct heat affected zone, which is costly and often overlooked. Welding process parameters, such as welding velocity and power input, are often not precisely known and they may vary during the deposition of the welds. In addition, the boundary conditions during the welding of actual structures are often uncertain. In the manufacturing of test specimens, it is possible to control and measure the welding conditions, thereby

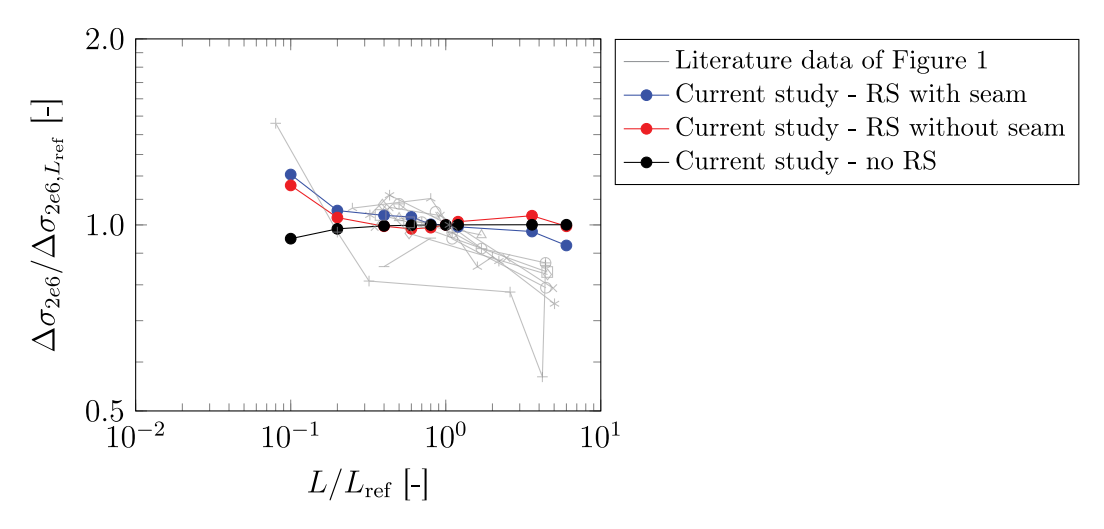


Fig. 19. Effect of specimen length on fatigue strength $\Delta \sigma_{2e6}$. $L_{ref} = 100$ mm.

reducing the uncertainties of most parameters. The validation study of Fig. 10 shows good agreement between the FE simulation and the residual stress measurement at the plate surface, indicating that the global behaviour of the welding process is at least reasonably captured. However, the local stress state, such as the weld toe location at the stress read-out points considered in this study, could not be validated due to a lack of experimental data. Residual stress measurements at the weld toe and below the surface are complex and difficult, if not impossible, to measure. Therefore, modelling approaches such as the one applied in this paper are currently the only possibility of obtaining residual stress results at these locations.

Due to the above-mentioned uncertainties, it is generally not yet accepted to include residual stresses from FE simulations in deterministic fatigue life assessments. However, the FE simulations can be applied for qualitative or relative comparisons, as used herein.

The resulting deformations after welding can cause angular misalignment of the specimens. The distribution of residual stress components might differ in a fatigue test compared to the simulations in this paper because the misalignment is reduced due to clamping the specimen in a fatigue test bench. Angular misalignments significantly affect fatigue resistance, but this is primarily due to the resulting increase in the stress range. The angular misalignment is deemed less important for the relative fatigue resistance of specimens with different lengths.

In the fracture mechanics simulation, the transverse residual stress field was altered to be symmetrical, with the largest value at the specimen center. This is an approximation that could influence the fatigue life. The interaction between a crack and the edge of the plate in determining K_I is reduced by shifting and symmetrizing the residual stress distribution around the centre of the specimen, which is unconservative. On the other hand, symmetrising the residual stress distribution using the side with the largest residual stresses as a basis is conservative. These effects are only relevant for relatively large fatigue cracks, which are rapidly propagating and therefore comprise only a small part of the fatigue life. Because these effects work in the opposite direction, and their individual contributions are marginal, the combined effect on the fatigue life is deemed negligible.

This paper considers the effect of cutting fatigue test specimens from a larger plate assembly for cruciform joints with a plate thickness of 12 mm and a single weld bead, loaded with a load ratio $R_{\rm load}=0.3$. For this geometry and load ratio, it is recommended to use a specimen length of at least 40 mm because the tests from the literature and the simulations in this paper show that shorter specimen lengths may provide overly optimistic fatigue resistance. This is to be considered an example; other specimen types, plate thicknesses, and stress ratios may have different lengths below which the specimens are no longer representative. Qualitatively, a similar trend of reduced fatigue resistance with increased specimen length is expected, caused by the relaxation of residual stress. Fatigue tests used to establish S-N curves are often conducted with $0.1 \le R_{\rm load} \le 0.3$, the specimens are often of limited thickness, and a correlation exists between the plate thickness and the number of weld passes per weld. The specimen length limit of 40 mm is therefore recommended for deriving S-N curves of joints with one weld pass. A shorter specimen length can be counterbalanced by a higher stress ratio of the applied stress, however, this has the disadvantage of inducing yielding at the local or meso scale in cases of large stress ranges.

5. Conclusions

In this study, the effect of cutting a larger welded plate assembly into smaller specimens on the residual stresses at the weld toe and the fatigue life of a cruciform joint is examined. Two variations are studied, namely, a geometry with a weld seam and a geometry without a weld seam. These variations are not exactly equal to a fillet weld and a full penetration weld because the heat input is considered to be equal for both variations. The welding process is simulated in FE models using a thermal and a mechanical analysis. Subsequently, the outer elements are stepwise inactivated to simulate the relaxation of residual stress caused by cutting

specimens from a larger welded plate assembly. The resulting residual stress fields are then incorporated into fatigue crack growth simulations using a mean stress correction in linear elastic fracture mechanics to assess their impact on fatigue life.

The study demonstrates that the finite element method can be used as a qualitative tool for evaluating the interplay between residual stress and fatigue performance, even though quantitative design applications remain limited due to modelling uncertainties. The findings show that residual stresses decrease with shorter specimen lengths due to reduced structural stiffness. The reduction of residual stresses in the longitudinal direction is more significant than in the transverse direction, however, it is of less interest for the investigated loading direction. The residual stresses in the transverse direction are larger for the model without seam than with seam but show a more distinct residual stress relaxation with decreasing specimen length. The relaxation of tensile residual stresses in the transverse direction leads to an increase in the fatigue life of shorter specimens. This effect is found to be small for specimens longer than 40 mm. The relation is found to be similar for the model with and without a seam, but the model with a seam shows a slightly larger effect of specimen length on the fatigue life. For cruciform joints with a single weld pass per weld, a minimum acceptable specimen length of 40 mm is therefore advised. The welding residual stress cannot explain a reduction in the fatigue life of long specimens (L > 200 mm) as observed in tests. This additional reduction is attributed to the statistical size effect.

Overall, the study underscores the importance of selecting appropriate specimen lengths in fatigue testing to ensure representative residual stress fields.

CRediT authorship contribution statement

Jorrit Rodenburg: Writing – original draft, Methodology, Formal analysis, Data curation, Conceptualization. **Henk Slot:** Writing – review & editing. **Sjoerd Hengeveld:** Writing – review & editing. **Johan Maljaars:** Writing – review & editing, Supervision, Methodology.

Declaration of competing interest

The authors declare that they have no known competing financial interests or personal relationships that could have appeared to influence the work reported in this paper.

Data availability

Data will be made available on request.

References

- [1] Dowling N. Mechanical behavior of materials. 4th ed. Pearson Education Limited; 2013.
- [2] Nitschke-Pagel T, Hensel J. An enhancement of the current design concepts for the improved consideration of residual stresses in fatigue-loaded welds. Weld World 2021;65:643–51.
- [3] Deinböck A, Hesse A, Wächter M, Hensel J, Esderts A, Dilger K. Increased accuracy of calculated fatigue resistance of welds through consideration of the statistical size effect within the notch stress concept, welding in the world. Weld World 2020;64:1725–36.
- [4] Baumgartner J, Bruder T, Hanselka H. Fatigue strength of laser beam welded automotive components made of thin steel sheets considering size effects. Int J Fatigue 2012;35:65–75.
- [5] Kuguel R. Relation between theoretical stress concentration factor Kt and fatigue notch factor Kf according to highly stressed volume approach. Tech. rep., Department of Theoretical and Applied Mechanics. College of Engineering. University of Illinois at Urbana-Champaign; 1960.
- [6] Sonsino C. Multiaxial fatigue of welded joints under in-phase and out-of-phase local strains and stresses. Int J Fatigue 1995;17(1):55-70.
- [7] Diemar A, Thumser R, Bergmann JW. Statistischer größeneinfluss und bauteilfestigkeit: Eine neue methode zur ermittlung von spannungsintegralen. Mater Test 2004;46(1–2):16–21. http://dx.doi.org/10.3139/120.100559.
- [8] Böhm J, Heckel K. Die vorhersage der dauerschwingfestigkeit unter berücksichtigung des statistischen größeneinflusses. Mater Werkst 1982;13(4):120-8.
- [9] Lundbäck A. In: Finite element modelling and simulation of welding of aerospace components, vol. 27, Lulea University of Technology; 2003.
- [10] Shakeri I, Shahani A, Rans C. Fatigue crack growth of butt welded joints subjected to mix mode loading and overloading. Eng Fract Mech 2021;241.
- [11] Aa E. Local cooling during welding: prediction and control of residual stresses and buckling distortion [Ph.D. thesis], Delft: Delft University of Technology; 2007.
- [12] Liang H, Kan Y, Chen H, Zhan R, Liu X, Wang D. Effect of cutting process on the residual stress and fatigue life of the welded joint treated by ultrasonic impact treatment. Int J Fatigue 2021;143:105998.
- [13] Altenkirch J, Steuwer A, Peel M, Withers P. The extent of relaxation of weld residual stresses on cutting out cross-weld test-pieces. Powder Diffr Suppl 2009;24:S31-6.
- [14] Jiang W, Woo W, An G-B, Park J-U. Neutron diffraction and finite element modeling to study the weld residual stress relaxation induced by cutting. Mater Des 2013:51:415–20.
- [15] Zhan R, Wang D, Ren Z, Deng C, Xu X, Liang H. Evolution of welding residual stresses involving the cutting process and its effect on fatigue performance. Int J Press Vessels Pip 2022:197:104636.
- [16] BS 7910:2019. Guide to methods for assessing the acceptability of flaws in metallic structures. BSI; 2019.
- [17] Malschaert D, Veljkovic M, Maljaars J. Numerical simulations of residual stress formation and its effect on fatigue crack propagation in a fillet welded T-joint. Eng Fract Mech 2024;306:110236.
- [18] Schijve J. Fatigue of Structures and Materials. Springer; 2009.
- [19] X-Ray diffraction. 2024, URL https://www.veqter.co.uk/residual-stress-measurement/x-ray-diffraction. [Accessed 26 August 2024].
- [20] Fitzpatrick M, Fry A, Holdway P, Kandil F, Shackleton J, Suominen L. Measurement good practice guide No. 52 Determination of residual stresses by X-ray Diffraction Issue 2. Tech. rep., National Physical Laboratory; 2005.
- [21] Mochizuki M, Hayashi M, Hattori T. Numerical analysis of welding residual stress and its verification using neutron diffraction measurement. Eng Mater Technol 2000;122:98–103.

- [22] Murakawa H, Deng D, Ma N, Wang J. Applications of inherent strain and interface element to simulation of welding deformation in thin plate structures. Comput Mater Sci 2012;51:43–52.
- [23] Kreuzer W, Heckel K. Prediction of fatigue strength of welded joints based on the statistical size. Mater Werkst 1999;30:87-94.
- [24] Xiao Z-G, Yamada K. A method of determining geometric stress for fatigue strength evaluation of steel welded joints. Int J Fatigue 2004;26:1277-93.
- [25] Maljaars J, Bonet E, Pijpers RJ. Fatigue resistance of the deck plate in steel orthotropic deck structures. Eng Fract Mech 2018;201:214-28.
- [26] Heinze C, Schwenk C, Rethmeier M. Influences of mesh density and transformation behavior on the result quality of numerical calculation of welding induced distortion. Simul Model Pr Theory 2011;19:1847–59.
- [27] Peric M, Nizetic S, Garasic I, Gubeljak N, Vuherer T, Tonkovic Z. Numerical calculation and experimental measurement of temperatures and welding residual stresses in a thick-walled T-joint structure. J Therm Anal Calorim 2020;141:313–22.
- [28] Zhu J, Khurshid M, Barsoum Z. Accuracy of computational welding mechanics methods for estimation of angular distortion and residual stresses. Weld World 2019;63:1391–405.
- [29] Goldak J, Chakravarti A, Bibby M. A new finite element model fo welding heat sources. Met Trans B 1984;15:299-305.
- [30] Rikken M, Pijpers R, Slot H, Maljaars J. A combined experimental and numerical examination of welding residual stresses. J Mater Process Technol 2018;261:98–106.
- [31] Chiocca A, Frendo F, Bertini L. Evaluation of heat sources for the simulation of the temperature distribution in gas metal arc welded joints. Metals 2019;9.
- [32] Fu G, Laurenco M, Duan M, Estefen S. Influence of the welding sequence on residual stress and distortion of fillet welded structures. Mar Struct 2016;46:30–55.
- [33] Spyridoni K. Prediction of residual stress of an orthotropic plate due to welding. Tech. rep., Delft University of Technology; 2019.
- [34] Berg N. Effects of residual stresses on the fatigue crack propagation of an orthotropic steel bridge deck. Tech. rep., Delft University of Technology; 2020.
- [35] Lundback A. Modelling and simulation of welding and metal deposition. [Ph.D. thesis], Lulea: Lulea University of Technology; 2010.
- [36] Long H, Gery A, Maropoulos P. Prediction of welding distortion in butt joint of thin plates. Mater Des 2009;30:4126-35.
- [37] Peric M, Tankovic A, Maksomivic K, Stamenkovic D. Numerical analysis of residual stresses in a T-joint fillet weld using a submodelling technique. FME Trans 2019;47:183–9.
- [38] Peric M, Tankovic A, Rodic A, Surjak M, Garisic I, Boras I, Svaic S. Numerical analysis and experimental investigation of welding residual stresses and distortions in a T-joint fillet weld. Mater Des 2014;53:1052–63.
- [39] Seles K, Peric M, Tonkovic Z. Numerical simulation of a welding process using a prescribed temperature approach. J Constr Steel Res 2018;145:49-57.
- [40] Barsoum Z. Residual stress analysis and fatigue of multi-pass welded tubular structures. Eng Fail Anal 2008;15:863-74.
- [41] Nguyen N, Ohta A, Matsuoka K, Suzuki N, Maeda Y. Analytical solutions for transient temperature of semi-infinite body subjected to 3-D moving heat sources. Weld Res Suppl 1999;265–74.
- [42] EN 1993-1-2:2011. Eurocode 3 Design of steel structures Part 1-2: General rules Structural fire design. CEN; 2011.
- [43] Sepe R, De Luca A, Greco A, Amentani E. Numerical evaluation of temperature fields and residual stresses in butt weld joints and comparison with experimental measurements. Fatigue Fract Eng Mater Struct 2021;44:182–98.
- [44] Bhatti A, Barsoum Z, Murakawa H, Barsoum I. Influence of thermo-mechanical material properties of different steel grades on welding residual stresses and angular distortion. Mater Des 2015;65:878–89.
- [45] Deng D. FEM prediction of welding residual stress and distortion in carbon steel considering phase transformation effects. Mater Des 2009;30:359-66.
- [46] Barsoum Z, Lundback A. Simplified FE welding simulation of fillet welds 3D effects on the formation residual stresses. Eng Fail Anal 2009;16:2281-9.
- [47] Koistinen D, Marburger R. A general equation prescribing extent of austenite-martensite transformation in pure iron-carbon alloys and plain carbon steel. Acta Metall 1959:7:50-60.
- [48] Watt D, Coon L, Bibby M, Goldak J, Henwood C. An algorithm for modeling microstructural development in weld heat-affected zones, (part A) reaction kinetics. Acta Metall 1988;36:3029–35.
- [49] Inoue T. Mechanics and characteristics of transformation plasticity and metallo-thermo-mechanical process simulation. Procedia Eng 2011;10:3793–8, 11th International Conference on the Mechanical Behavior of Materials (ICM11).
- [50] Leblond J. Mathematical modelling of transformation plasticity in steels II: Coupling with strain hardening phenomena. Int J Plast 1989;5(6):573–91.
- [51] Fischer F, Reisner G, Werner E, Tanaka K, Cailletaud G, Antretter T. A new view on transformation induced plasticity (TRIP). Int J Plast 2000;16(7):723-48.
- [52] Barsoum Z, Barsoum I. Residual stress effects on fatigue life of welded structures using LEFM. Eng Fail Anal 2009;16:449-67.
- [53] Heinze C, Pittner A, Rethmeier M, Babu S. Dependency of martensite start temperature on prior austenite grain size and its influence on welding-induced residual stresses. Comput Mater Sci 2013;69:251–60.
- [54] Suman S, Biswas P. Comparative study on SAW welding induced distortion and residual stresses of CSEF steel considering solid state phase transformation and preheating. J Manuf Process 2020;51:19–30.
- [55] Mullins J, Gunnars J. ReSearch 2009:16 Influence of Hardening Model on Weld Residual Stress Distribution. Tech. rep., Stockholm: Swedish Radiation Safety Authority: 2009.
- [56] Elcoate C, Dennis R, Bouchard P, Smith M. Three dimensional multi-pass repair weld simulations. Int J Press Vessels Pip 2005;82:244-57.
- [57] Huang X, Moan T. Improved modeling of the effect of R-ratio on crack growth rate. Int J Fatigue 2007;29:591-602.
- [58] Hensel J, Nitschke-Pagel T, Tchoffo Ngoula D, Beier H-T, Tchuindjang D, Zerbst U. Welding residual stresses as needed for the prediction of fatigue crack propagation and fatigue strength. Eng Fract Mech 2018;198:123–41, Fracture mechanics-based determination of the fatigue strength of weldments.
- [59] Hensel J. Mean stress correction in fatigue design under consideration of welding residual stress. Weld World 2020;64:535-44.
- [60] Maljaars J, Leander J, Nussbaumer A, Sørensen JD, Straub D. Models and methods for probabilistic safety assessment of steel structures subject to fatigue. Struct Saf 2025;102446.
- [61] Newman J, Raju I. Stress intensity factor equations for cracks in three-dimensional finite bodies. In: Fracture mechanics: proceedings of the 14th symposium. vol. I: theory and anlysis. STP 791. Philadelphia: ASTM; 1983, p. 238–65.
- [62] Bowness D, Lee M. Fracture mechanics assessment of fatigue cracks in offshore tubular structures. Tech. rep, London: HSE Offshore Technology Report for HSE, EPSRC, and Chevron Oil; 2002.
- [63] Fett T, Munz D, Neumann J. Local stress intensity factors for surface cracks in plates under power-shaped stress distributions. Eng Fract Mech 1990;36:647–51.
- [64] Caprace J-D, Fu G, Carrara JF, Remes H, Shin SB. A benchmark study of uncertainness in welding simulation. Mar Struct 2017;56:69-84.